

Fully HOC Scheme for Mixed Convection Flow in a Lid-Driven Cavity Filled with a Nanofluid

Dingfang Li¹, Xiaofeng Wang^{1,2,*} and Hui Feng¹

¹ School of Mathematics and Statistics, Wuhan University, Wuhan 430072, Hubei, China

² Department of Mathematics, Henan Institute of Science and Technology, Xinxiang 453003, Henan, China

Received 31 December 2010; Accepted (in revised version) 26 July 2012

Available online 25 January 2013

Abstract. A fully higher-order compact (HOC) finite difference scheme on the 9-point two-dimensional (2D) stencil is formulated for solving the steady-state laminar mixed convection flow in a lid-driven inclined square enclosure filled with water- Al_2O_3 nanofluid. Two cases are considered depending on the direction of temperature gradient imposed (Case I, top and bottom; Case II, left and right). The developed equations are given in terms of the stream function-vorticity formulation and are non-dimensionalized and then solved numerically by a fourth-order accurate compact finite difference method. Unlike other compact solution procedure in literature for this physical configuration, the present method is fully compact and fully higher-order accurate. The fluid flow, heat transfer and heat transport characteristics were illustrated by streamlines, isotherms and averaged Nusselt number. Comparisons with previously published work are performed and found to be in excellent agreement. A parametric study is conducted and a set of graphical results is presented and discussed to elucidate that significant heat transfer enhancement can be obtained due to the presence of nanoparticles and that this is accentuated by inclination of the enclosure at moderate and large Richardson numbers.

AMS subject classifications: 35K57, 65N06, 76T20

Key words: HOC difference scheme, pseudo-time derivative, mixed convection, ADI method.

1 Introduction

Suspensions of colloidal particles dubbed as nanofluids was pioneered by Choi [1], in which small amounts of metallic or metallic oxide nanoparticles are dispersed into wa-

*Corresponding author.

Email: dfli@whu.edu.cn (D. F. Li), wangxiaofeng1166@163.com (X. F. Wang), hfeng.math@whu.edu.cn (H. Feng)

ter and other fluids. The nanofluid does not simply refer to a liquid-solid mixture, and some special requirements are necessary, such as even suspension, stable suspension, durable suspension, low agglomeration of particles, and no chemical change of the fluid. Various types of powders such as metallic, non-metallic and polymeric particles can be added into fluids to form slurries. In conventional cases, the suspended particles are of μm or even nm dimensions [2]. It has been shown experimentally [3, 4] that nanofluids can have anomalously higher thermal conductivities than that of the base fluid, thus posing as a promising alternative for thermal applications. The convective heat transfer characteristic of nanofluids depends on the thermo-physical properties of the base fluid and the ultra fine particles, the flow pattern and flow structure, the volume fraction of the suspended particles, the dimensions and the shape of these particles [5]. The utility of a particular nanofluid for a heat transfer application can be established by suitably modeling the convective transport in the nanofluid [6]. As revealed in the recent comprehensive reviews [7, 8], over the past decade there have been tremendous attempts to identify and model mechanisms of thermal conductivity enhancement of nanofluids, including size and shape of the nanoparticles, the hydrodynamic interaction between nanoparticles and base fluid, clustering of particles, temperature or Brownian motion, and so on. Khanafer et al. [9] investigated the problem of buoyancy-driven heat transfer enhancement of nanofluids in a 2D enclosure. Jou and Tzeng [10] reported a numerical study of the heat transfer performance of nanofluids inside 2D rectangular enclosures. Their results indicated that increasing the volume fraction of nanoparticles produced a significant enhancement of the average rate of heat transfer.

Mixed convection flow and heat transfer in enclosures is of interest in engineering and science. Its applications include nuclear reactors, lakes and reservoirs, solar collectors and crystal growth. Moreover, the flow and heat transfer in a shear driven cavity arises in industrial processes such as food processing and float glass production [11, 12]. Combination of buoyancy forces due to the temperature gradient and forced convection due to shear forces results in a mixed convection heat transfer situation, which is a complex phenomenon due to the interaction of these forces. Numerous studies on single or double lid-driven cavity flow and heat transfer involving different cavity configurations, various pure fluids and imposed temperature gradients have been continually published in the literature. Both thermally stable and unstable lid-driven flows inside enclosures have been investigated numerically by Torrance et al. [13] for fixed values of Reynolds and Prandtl numbers. Their numerical results have indicated that the Richardson number is a controlling parameter for the problem. Later on, Iwatsu et al. [14] have studied numerically mixed convection heat transfer in a driven cavity with a stable vertical temperature gradient. Their results have shown that the flow features are similar to those of a conventional driven-cavity of a non-stratified fluid for small values of the Richardson number. All of the above mixed convection studies were done for a pure base fluid without nanoparticles. A literature survey indicates that few studies have been done on mixed convection in a lid-driven cavity for a nanofluid compared to the natural convection case [5]. For example, Tiwari and Das [15] investigated numerically heat transfer

augmentation in a lid-driven cavity filled with a nanofluid and found that the presence of nanoparticles in a base fluid is capable of increasing the heat transfer capacity of the base fluid. Muthamilselvan et al. [16] reported on the heat transfer enhancement of copper-water nanofluids in a lid-driven enclosure with different aspect ratios. Recently, Abu-Nada et al. [5] studied the numerical modeling of steady laminar mixed convection flow in a lid-driven inclined square enclosure filled with water- Al_2O_3 nanofluid using a second-order accurate finite-volume method.

This work is focused on the fully compact fourth-order scheme for mixed convection flow in a lid-driven cavity filled with a water- Al_2O_3 nanofluid using the widely used Boussinesq model [5]. In particular, a compact fourth-order accurate Neumann boundary condition has been developed for temperature at the adiabatic walls. The treatment of the derivative source term is also compact and has been done in such a way as to give fourth-order accuracy and easy assimilation with the solution procedure. As expected, the results are very accurate and even coarse grid (61×61) results compare very well with previous computations. A parametric study is conducted and a set of graphical results is presented and discussed to illustrate the effects of the presence of nanoparticles and enclosure inclination angle on the flow and heat transfer characteristics. Overall, besides opening up new possibilities, the method may be considered an efficient one for computation of flow for this physical configuration.

This paper has been arranged in eight sections: Section 2 deals with the problem, the governing equations and their nondimensionalizations; Sections 3-4 with the HOC discretization and related boundary conditions; Section 5 with the pseudo-time numerical method; and Sections 6-7 with the results and discussion and the last section, conclusions.

2 Problem description

A 2D steady mixed convection in a lid-driven inclined square enclosure filled with a nanofluid is considered for the present study, the inclination angle is γ . The nanofluid in the cavity is modeled as a dilute solid-liquid mixture with a uniform volumetric fraction θ of nanoparticles (Al_2O_3) dispersed within a base fluid (water). The nanofluid is assumed incompressible and the flow is conceived as laminar. It is idealized that water and nanoparticles are in thermal equilibrium and no slip occurs between the two media. The thermo-physical properties of the nanofluid are assumed to be constant except for the density variation, which is approximated by the Boussinesq model [5]. The model configuration and boundary conditions are considered in Fig. 1 for two cases studied. For both of the two cases, the top wall is moving from left to right at a constant speed. In case I, the temperature at the top side wall is higher than that at the bottom side wall while the vertical side walls are thermally insulated. In such a case, a gravitationally-stable upward temperature gradient is established and the heat transfer within the cavity is mainly through conductive mode if the top wall is stationary [17]. This case is similar to that studied by Iwatsu et al. [18]. In case II, the temperature at the left side wall

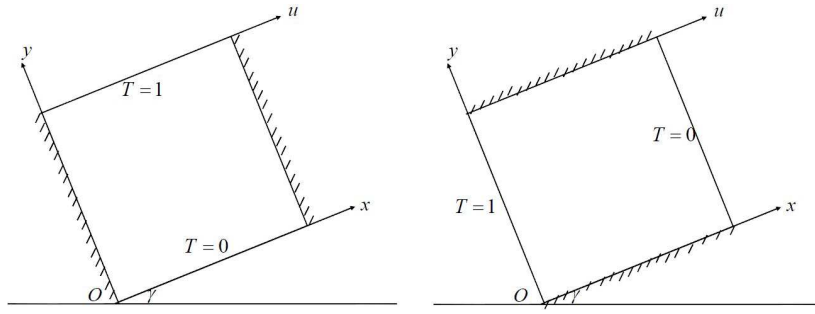


Figure 1: Physical model and boundary conditions for two cases.

is higher than that at the right side wall while the top and bottom walls are thermally insulated. The imposed leftward temperature gradient would result in a clockwise recirculation due to natural convection if the top wall is stationary, and it would assist the buoyancy if the top wall is sliding.

Invoking the foregoing assumptions, the conservation of mass, momentum, and energy for the 2D, laminar, steady state mixed convection flow in the cavity is expressed in terms of stream-function ψ , vorticity ω and temperature T . The resulting governing equations are cast in dimensionless form as follows:

$$\nabla^2 \psi + \omega = 0, \quad (2.1a)$$

$$\nabla^2 T - K(\mathbf{U} \cdot \nabla T) = 0, \quad (2.1b)$$

$$\nabla^2 \omega - \chi_1(\mathbf{U} \cdot \nabla \omega) + \chi_2 \left(\frac{\partial T}{\partial x} \cos \gamma - \frac{\partial T}{\partial y} \sin \gamma \right) = 0, \quad (2.1c)$$

where

$$\mathbf{U} = (u, v), \quad u = \frac{\partial \psi}{\partial y}, \quad v = -\frac{\partial \psi}{\partial x}, \quad \omega = \frac{\partial v}{\partial x} - \frac{\partial u}{\partial y},$$

$$\chi_1 = Re(1-\theta)^{2.5} \left(1 - \theta + \frac{\theta \rho_p}{\rho_f} \right), \quad \chi_2 = Ri \left(1 - \theta + \frac{\theta \beta_p}{\beta_f} \right) \chi_1,$$

$$K = Pr Re \left(1 - \theta + \frac{\theta (\rho c_p)_p}{(\rho c_p)_f} \right) \frac{\kappa_f}{\kappa_m}, \quad \frac{\kappa_f}{\kappa_m} = \frac{\kappa_p + 2\kappa_f + \theta(\kappa_f - \kappa_p)}{\kappa_p + 2\kappa_f - 2\theta(\kappa_f - \kappa_p)},$$

u and v are the components of the velocity in x - and y - directions, respectively, κ is thermal conductivity, β is the thermal expansion coefficient, c_p is the specific heat at constant pressure. The thermophysical properties chosen in this study for the nanofluid belong to water and Al_2O_3 , the numerical data were evaluated as such [19]:

- Water: $c_p = 4179$, $\rho = 997.1$, $\kappa = 0.613$, $\beta = 2.1 \times 10^{-4}$;
- Al_2O_3 : $c_p = 765$, $\rho = 3970$, $\kappa = 25$, $\beta = 8.5 \times 10^{-6}$.

The dimensionless parameters pertinent to the present problem thus include: the Reynolds number Re , the Prandtl number Pr , the Grashof number Gr and the Richardson number Ri , where $Ri = Gr/Re^2$. The subscripts p , f and m denote, the nanoparticles, the base fluid and the nanofluid, respectively. The boundary conditions applied to the computational domain are given as follows:

- Velocity: $u = 1$ on the top wall and $u = 0$ on the rest of walls, $v = 0$ on all walls;
- Streamfunction: $\partial\psi/\partial n = 1$ on the top wall and $\partial\psi/\partial n = 0$ on the rest of walls, $\psi = 0$ on all walls, where n indicates the normal direction to the wall surface;
- Vorticity: $w = -\partial^2\psi/\partial n^2$ on all walls;
- Temperature: $T = 1$ at hot wall, $T = 0$ at cold wall, and $\partial T/\partial n = 0$ on adiabatic wall.

3 HOC difference scheme

HOC finite difference schemes, which feature higher-order accuracy and spectral-like resolution with smaller stencils and easier application of boundary conditions, has attracted more and more interest and attention. To develop a HOC finite difference scheme, the given domain is covered by a uniform mesh in both x - and y -directions:

$$x_i = ih, \quad y_j = jh, \quad i, j = 0, 1, 2, \dots, M-1, M,$$

with mesh size $h = 1/M$ and M is a preassigned positive integer. In this section we formulate a fully fourth-order compact approximation that can solve Eqs. (2.1a)-(2.1c) subject to the boundary conditions with the novelty of genuine compactness, i.e., the compact scheme is strictly within the following 9-point stencil, (x_i, y_j) , (x_{i+1}, y_j) , (x_{i-1}, y_j) , (x_i, y_{j-1}) , (x_i, y_{j+1}) , (x_{i+1}, y_{j+1}) , (x_{i-1}, y_{j+1}) , (x_{i-1}, y_{j-1}) and (x_{i+1}, y_{j-1}) . Note that each of these Eqs. (2.1a)-(2.1c) is a special case of the following 2D convection-diffusion equation for a transport variable ϕ ($\phi = \psi, \omega, T$):

$$\nabla^2\phi - a\frac{\partial\phi}{\partial x} - b\frac{\partial\phi}{\partial y} + f = 0, \quad (3.1)$$

where a, b are the variable or constant convective coefficients and f is a forcing function. The 9-point variable coefficient HOC difference scheme of Spatz and Carey [20], originally used for the ψ - ω formulation of the 2D steady-state N-S equation, forms the core of the discretization of the present study. This HOC scheme has been obtained from the second-order central difference scheme by approximating the derivatives appearing in the second-order truncation error terms through the use of the original partial differential equation itself [21]. The HOC difference approximation of Eq. (3.1) at (i, j) is given by [22]

$$A^\phi\phi_{xx} + B^\phi\phi_{yy} - C^\phi\phi_x - D^\phi\phi_y + F^\phi = 0, \quad (3.2)$$

where ϕ_x , ϕ_y and ϕ_{xx} , ϕ_{yy} are the first- and second-order central difference formulas in the x - and y -directions, respectively, and the coefficients are as follows:

$$\begin{aligned} A^\phi &= 1 + H(a^2 - 2a_x), & C^\phi &= a + H(a_{xx} + a_{yy} - aa_x - ba_y), \\ B^\phi &= 1 + H(b^2 - 2b_y), & D^\phi &= b + H(b_{xx} + b_{yy} - ab_x - bb_y), \\ F^\phi &= f + H(f_{xx} + f_{yy} - af_x - bf_y - 2(a_y - ab + b_x)\phi_{xy} + 2(\phi_{xxyy} - a\phi_{xyy} - b\phi_{xxy})), \end{aligned}$$

where $H = h^2/12$. Here it is assumed that the forcing function f and its derivatives are known analytically or their discrete approximations are known.

For the stream-function equation (2.1a), ϕ , a , b and f in Eq. (3.1) are replaced by ψ , 0, 0 and ω , respectively, and then the corresponding coefficients can be rewritten as:

$$A^\psi = B^\psi = 1, \quad C^\psi = D^\psi = 0, \quad F^\psi = \omega + H(\omega_{xx} + \omega_{yy} + 2\psi_{xxyy}).$$

For the energy equation (2.1b), ϕ , a , b and f in Eq. (3.1) are replaced by T , $K\partial\psi/\partial y$, $-K\partial\psi/\partial x$ and 0, respectively, and then the corresponding coefficients can be rewritten as:

$$\begin{aligned} A^T &= 1 + HK(K\psi_y\psi_y - 2\psi_{xy}), & C^T &= HK(K\psi_x\psi_{yy} - K\psi_y\psi_{xy} - \omega_y) + K\psi_y, \\ B^T &= 1 + HK(K\psi_x\psi_x + 2\psi_{xy}), & D^T &= HK(\omega_x - K\psi_x\psi_{xy} + K\psi_y\psi_{xx}) - K\psi_x, \\ F^T &= 2H(T_{xxyy} + K\psi_xT_{xxy} - K\psi_yT_{xyy} - KT_{xy}(\psi_{yy} + K\psi_x\psi_y - \psi_{xx})). \end{aligned}$$

For the vorticity equation (2.1c), ϕ , a , b and f in Eq. (3.1) are replaced by ω , $\chi_1\partial\psi/\partial y$, $-\chi_1\partial\psi/\partial x$ and $\chi_2(\partial T/\partial x \cos\gamma - \partial T/\partial y \sin\gamma)$, respectively. The forcing function in the vorticity equation is not explicitly known and is in derivative form. It may be mentioned that in the earlier HOC simulation of the present physical configuration [23], although the overall accuracy of the scheme was fourth, this particular source term was approximated using the standard central difference scheme at most of the points. In the following, we proceed to obtain a HOC accurate approximation of this term applying the same mechanism of using the original partial differential equation. Assuming the temperature T to be smooth, the finite difference approximations of first-derivatives appearing in the forcing function are given as follows [24]:

$$\frac{\partial T}{\partial x} = T_x - 2H \frac{\partial^3 T}{\partial x^3} + \mathcal{O}(h^4). \quad (3.3)$$

From the energy equation (2.1b), we can obtain

$$\frac{\partial^3 T}{\partial x^3} = K(\psi_{xy}T_x + \psi_yT_{xx} - \psi_{xx}T_y - \psi_xT_{xy}) - T_{xxyy} + \mathcal{O}(h^2). \quad (3.4)$$

Substituting Eq. (3.4) into Eq. (3.3) yields

$$\frac{\partial T}{\partial x} = \delta_x T - 2HK(\psi_{xy}T_x + \psi_yT_{xx} - \psi_{xx}T_y - \psi_xT_{xy}) + 2HT_{xxyy} + \mathcal{O}(h^4).$$

Similarly, we can get

$$\frac{\partial T}{\partial y} = \delta_y T - 2HK(\psi_{yy}T_x + \psi_y T_{xy} - \psi_{xy}T_y - \psi_x T_{yy}) + 2HT_{xxy} + \mathcal{O}(h^4).$$

Then the corresponding coefficients can be rewritten as:

$$\begin{aligned} A^\omega &= 1 + H\chi_1(\chi_1\psi_y\psi_y - 2\psi_{xy}), \\ B^\omega &= 1 + H\chi_1(\chi_1\psi_x\psi_x + 2\psi_{xy}), \\ C^\omega &= H\chi_1(\chi_1\psi_x\psi_{yy} - \chi_1\psi_y\psi_{xy} - \omega_y) + \chi_1\psi_y, \\ D^\omega &= H\chi_1(\omega_x - \chi_1\psi_x\psi_{xy} + \chi_1\psi_y\psi_{xx}) - \chi_1\psi_x, \\ F^\omega &= \chi_2(T_x \cos \gamma - T_y \sin \gamma) + 2H(\omega_{xxyy} - \chi_1\psi_y\omega_{xyy} + \chi_1\psi_x\omega_{xxy}) \\ &\quad + 2H(\chi_2(T_{xyy} \cos \gamma - T_{xxy} \sin \gamma) - \chi_1(\psi_{yy} + \chi_1\psi_x\psi_y - \psi_{xx})\omega_{xy}) \\ &\quad - \chi_2H(K + \chi_1)(\cos \gamma \psi_y T_{xx} + \sin \gamma \psi_x T_{yy} - (\psi_y \sin \gamma + \psi_x \cos \gamma)T_{xy}) \\ &\quad - \chi_2HK((\cos \gamma \psi_{xy} - \sin \gamma \psi_{yy})T_x + (\psi_{xy} \sin \gamma - \psi_{xx} \cos \gamma)T_y). \end{aligned}$$

It may be mentioned that the treatment of the first-order derivative source term mentioned earlier can easily be extended to second-order derivatives as well. The more important point is that through this source term treatment, an HOC scheme for the primitive variable form of the 2D N-S equations can be constructed as the pressure gradient term in the momentum equation and the source term in the pressure Poisson equation can now be handled [21].

4 HOC wall boundary conditions

The lid-driven cavity problem has been frequently used as a test problem for assessing the performance of numerical solution techniques. The implementation of numerical boundary conditions has received considerable attention in the past [25, 26]. In this section, we shall present a HOC difference formula for the cavity problem on the boundary. The boundary conditions for case I and case II are shown in Table 1.

Table 1: The boundary conditions for case I and case II.

Boundary	Case I	Case II
$y = 1$	$\psi = 0, \partial\psi/\partial y = 1, T = 1$	$\psi = 0, \partial\psi/\partial y = 1, \partial T/\partial y = 0$
$y = 0$	$\psi = 0, \partial\psi/\partial y = 0, T = 0$	$\psi = 0, \partial\psi/\partial y = 0, \partial T/\partial y = 0$
$x = 0$	$\psi = 0, \partial\psi/\partial x = 0, \partial T/\partial x = 0$	$\psi = 0, \partial\psi/\partial x = 0, T = 1$
$x = 1$	$\psi = 0, \partial\psi/\partial x = 0, \partial T/\partial x = 0$	$\psi = 0, \partial\psi/\partial x = 0, T = 0$

For case I, the stream-function ψ equals zero on the boundaries. At the corners, both u and v do not vary in the x - and y -directions and, therefore, the vorticity ω is equal to

zero. At the left boundary, employing a Taylor series expansion, we get

$$0 = \frac{\partial \psi_{0,j}}{\partial x} = \delta_x^+ \psi_{0,j} - \frac{h}{2} \frac{\partial^2 \psi_{0,j}}{\partial x^2} - 2H \frac{\partial^3 \psi_{0,j}}{\partial x^3} - \frac{h^3}{24} \frac{\partial^4 \psi_{0,j}}{\partial x^4} + \mathcal{O}(h^4),$$

where δ_x^+ is the first-order forward difference operator. Also in view of the fact that

$$\omega_{0,j} = -\frac{\partial^2 \psi_{0,j}}{\partial x^2}, \quad \frac{\partial^2 \omega_{0,j}}{\partial x^2} = -\chi_2 \left(\frac{\partial T_{0,j}}{\partial x} \cos \gamma - \frac{\partial T_{0,j}}{\partial y} \sin \gamma \right) - \frac{\partial^2 \omega_{0,j}}{\partial y^2},$$

we get the fourth-order accuracy $\mathcal{O}(h^4)$ expression as follows:

$$0 = \delta_x^+ \psi_{0,j} + \frac{h}{2} \omega_{0,j} + 2H \delta_x^+ \omega_{0,j} + \frac{h^3}{24} (\chi_2 (\cos \gamma \delta_x^+ - \sin \gamma \delta_y) T + \delta_y^2 \omega)_{0,j},$$

that is

$$\begin{aligned} \omega_{0,j} = & -\frac{h}{12} \chi_2 (2 \cos \gamma (T_{1,j} - T_{0,j}) - \sin \gamma (T_{0,j+1} - T_{0,j-1})) \\ & - \frac{4}{h^2} \psi_{1,j} - \frac{2}{3} \omega_{1,j} - \frac{1}{6} (\omega_{0,j+1} + \omega_{0,j-1}). \end{aligned}$$

Similarly, we can get ω on the other three boundary walls.

On the insulated left and right walls, we now proceed to develop a fourth-order accurate $\mathcal{O}(h^4)$ zero-gradient temperature boundary condition. It may be mentioned that as temperature remains constant on the horizontally walls, this zero-gradient condition is automatically satisfied at the corners [21]. On the left wall, employing a Taylor series expansion, we get

$$0 = \frac{\partial T_{0,j}}{\partial x} = \left(T_x - 2H \frac{\partial^3 T}{\partial x^3} \right)_{0,j} + \mathcal{O}(h^4).$$

Also in view of the fact that

$$\nabla^2 T_{0,j} = 0, \quad \frac{\partial^3 T_{0,j}}{\partial x^3} = -\frac{\partial^3 T_{0,j}}{\partial y^2 \partial x},$$

we can get the fourth-order accuracy $\mathcal{O}(h^4)$ expression

$$0 = (T_x + 2HT_{xyy})_{0,j},$$

that is

$$T_{1,j+1} + T_{1,j-1} - T_{-1,j+1} - T_{-1,j-1} + 4(T_{1,j} - T_{-1,j}) = 0.$$

Again the fourth-order compact difference discretization of the energy equation $\nabla^2 T_{0,j} = 0$ is given by [27]

$$T_{1,j+1} + T_{1,j-1} + T_{-1,j+1} + T_{-1,j-1} + 4(T_{0,j+1} + T_{1,j} + T_{0,j-1} + T_{-1,j}) = 20T_{0,j}.$$

From the above two equation, we can get the boundary condition on the left wall

$$T_{0,j} = \frac{1}{10}(T_{1,j+1} + T_{1,j-1} + 2T_{0,j+1} + 4T_{1,j} + 2T_{0,j-1}),$$

and on the right wall

$$T_{M,j} = \frac{1}{10}(T_{M-1,j+1} + T_{M-1,j-1} + 2T_{M,j+1} + 4T_{M-1,j} + 2T_{M,j-1}).$$

This approach used to develop the temperature boundary conditions on the insulated walls can also be extended to similar physical situations for a flow variable ϕ , where, on the boundary, $\partial\phi/\partial n = 0$ and $\nabla^2\phi = 0$, where n is the direction normal to the boundary. Similarly, we can get the HOC wall boundary conditions for case II.

5 Pseudo-time method

The new HOC scheme (3.2) is fourth-order accurate to Eq. (3.1), therefore, they need to be solved in an iterative manner such as SOR, ADI, factorization schemes, pseudo time iterations, etc.. Recently Erturk et al. [28] have presented a new, stable and efficient numerical method that solve the stream-function and vorticity equations. The numerical method solve the governing steady equations through iterations in the pseudo-time. Assigning pseudo-time derivatives to Eq. (3.2), we have the following form:

$$\frac{\partial\phi}{\partial t} = A^\phi\delta_x^2\phi + B^\phi\delta_y^2\phi - C^\phi\delta_x\phi - D^\phi\delta_y\phi + F^\phi, \quad (5.1)$$

where δ_x, δ_y and δ_x^2, δ_y^2 are the first- and second-order central difference operators in the x - and y -directions, respectively.

We solve these Eq. (5.1) in the pseudo-time domain until the solutions converge to the steady state and the numerical methods we will use is the alternating direction implicit (ADI) method. The ADI method is a very widely used numerical method and in this method a 2D problem is solved in two sweeps while solving the equation implicitly in 1D in each sweep [24, 32]. The advantage of the ADI method is that each equation requires the solution of tri-diagonal systems, which is computationally very efficient using the Thomas algorithm. When we apply the ADI method to solve Eq. (5.1), first we solve the following tri-diagonal system in the x -direction:

$$\left(1 - \frac{\tau}{2}A^\phi\delta_x^2 + \frac{\tau}{2}C^\phi\delta_x\right)\phi^* = \phi^n + \frac{\tau}{2}B^\phi\delta_y^2\phi^n - \frac{\tau}{2}D^\phi\delta_y\phi^n + \frac{\tau}{2}F^\phi,$$

where ϕ^* is the introduced variables, τ is the time mesh size. Then we solve the following tri-diagonal system in the y -direction:

$$\left(1 - \frac{\tau}{2}B^\phi\delta_y^2 + \frac{\tau}{2}D^\phi\delta_y\right)\phi^{n+1} = \phi^* + \frac{\tau}{2}A^\phi\delta_x^2\phi^* - \frac{\tau}{2}C^\phi\delta_x\phi^* + \frac{\tau}{2}F^\phi.$$

After solving for ψ, ω , the velocities u, v at a grid point (i, j) are calculated from the discrete approximation of Eq. (5.1). The following approximations are compact and have a local truncation error of order $\mathcal{O}(h^4)$ [33]:

$$\begin{aligned} u_{i,j} &= \frac{2}{3}\delta_y\psi_{i,j} + \frac{1}{6}\delta_y(\psi_{i+1,j} + \psi_{i-1,j}) + 2H\delta_y\omega_{i,j}, \\ v_{i,j} &= -\frac{2}{3}\delta_x\psi_{i,j} - \frac{1}{6}\delta_x(\psi_{i,j+1} + \psi_{i,j-1}) - 2H\delta_x\omega_{i,j}. \end{aligned}$$

Moreover, the most important characteristic of the problem is the rate of heat transfer across the cavity, which is described by the Nusselt number. The local Nusselt number along the isothermal walls of the cavity are expressed as follows [17]:

$$Nu(x) = -\frac{\kappa_m}{\kappa_f} \frac{\partial T}{\partial y} \Big|_{y=0,1}, \quad Nu(y) = -\frac{\kappa_m}{\kappa_f} \frac{\partial T}{\partial x} \Big|_{x=0,1}.$$

The average Nusselt number along the isothermal walls is:

$$\overline{Nu} = \int_0^1 Nu(x) dx, \quad \overline{Nu} = \int_0^1 Nu(y) dy.$$

The total heat transfer rate across the whole cavity is the sum of the average Nusselt numbers over all sources or sinks.

6 Grid testing and code validation

In this study, in all of the cases considered, we start the iterations from a homogeneous initial guess and continue until a certain condition of convergence is satisfied. The above process is repeated until the following convergence criterion for stream-function ψ , vorticity ω and temperature T is satisfied:

$$\max(|\phi^{n+1} - \phi^n|) < 10^{-6}. \quad (6.1)$$

At this convergence level, this would indicate that the variables ψ , ω and T are changing less than 0.0001% of their value between two iterations at every grid point in the mesh. To test and assess grid independence of the solution scheme, various mesh combinations were explored for the Al_2O_3 -water nanofluid. The present code was tested for grid independence by calculating the average Nusselt number on the left wall and the values of ψ and ω on the primary vortex for case II in Table 2. It is seen from this table that the present results for 61×61 grids give grid-independent results as verified and mentioned above.

In order to verify the accuracy of the present numerical study, the present numerical procedure was validated by performing simulations for the classical lid-driven square cavity problem. This problem is of great importance because it displays almost all

Table 2: Grid independence study for a nanofluid, $Ri=100$, $\theta=10\%$, $\gamma=0^\circ$.

Grids	ψ_{\max}	ω	\overline{Nu}	Grids	ψ_{\max}	ω	\overline{Nu}
19×19	0.207891	5.006223	1.480955	61×61	0.207421	4.957780	1.443260
25×25	0.207376	4.926866	1.467591	67×67	0.207401	4.971265	1.441801
31×31	0.207680	4.967942	1.459473	73×73	0.207347	4.949045	1.440589
43×43	0.207478	4.950048	1.450183	85×85	0.207339	4.971641	1.438692
55×55	0.207400	4.984601	1.445048	97×97	0.207328	4.963844	1.437276

Table 3: Comparison of the values and locations on the primary vortex for $Re=1000$.

Reference	Grids	ψ	ω	x	y
Erturk and Gökcöl [24]	601×601	0.118938	2.067760	0.53000	0.5650
Ghia et al. [35]	128×128	0.117929	2.049680	0.46870	0.5625
Zhang [36]	128×128	0.118806	2.066777	0.46875	0.5625
Botella and Peyret [37]	128×128	0.118937	2.067750	0.46920	0.5652
Bruneau and Saad [38]	128×128	0.117860	2.050800	0.46875	0.5625
Bruneau and Saad [38]	1024×1024	0.118920	2.067400	0.46875	0.5654
Cheng et al. [17]	128×128	0.116874	2.064753	0.46875	0.5625
Present Study	61×61	0.117402	2.058175	0.53333	0.5667

the fluid mechanical phenomena for incompressible viscous flows in a simplest geometry [34] and it is frequently used for the assessment of numerical methods, particularly the benchmark solutions of the incompressible fluid flows governed by the N-S equations [17,24,35–38]. For this problem, only Eqs. (2.1a) and (2.1c) are solved in the absence of the nanoparticles and heat generation and the last term in Eq. (2.1c) is discarded. The top wall is moving in the positive x -direction and the remaining three walls are stationary. Computed results of stream-function and vorticity contours for $Re=1000,1500$ are depicted in Fig. 2 and comparisons of our calculated values of stream-function, vorticity and location on the primary vortex with the reported benchmark solutions are listed in Table 3. Furthermore, Fig. 3 shows that the profiles of the horizontal velocity u and the vertical velocity v at the mid-sections of the cavity of the present solution compare well with those reported by Erturk et al. [24]. All of these favorable comparisons lend confidence in the accuracy of the numerical results of the present work.

7 Results and discussion

In this section, the numerical results for mixed convection heat transfer of a water- Al_2O_3 nanofluid in a lid-driven cavity are discussed. The non-dimensional controlling parameters for this investigation are the Richardson number Ri , the cavity inclination angle γ and the nanoparticles volume fraction θ . Throughout the study, the Prandtl number $Pr=6.2$ is fixed. The Grashof number Gr is set to 100 and the value of Ri is varied from 0.01 to 100 to cover a wide range of Richardson number.

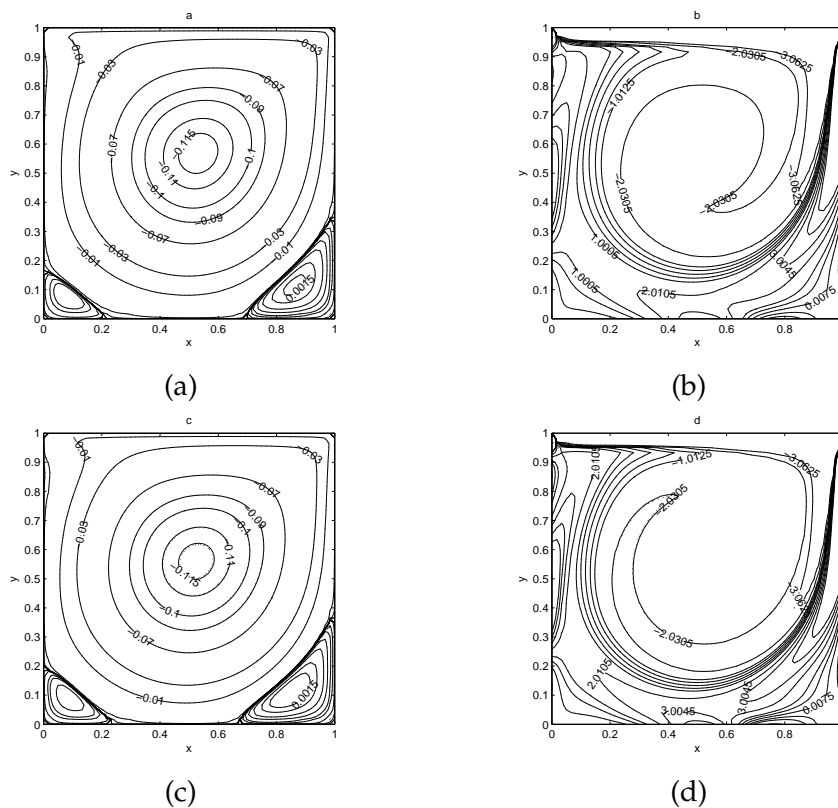


Figure 2: Comparison of the streamlines distributions and vorticity contours between the present study (—) in the absence of nanoparticles and internal heat generation and Erturk et al. [24] (···) for $Re=1000$ (a), (b) $Re=1500$ (c), (d). For the present study: $|\psi_{\max}|_{Re=1000}=0.117402$, $|\psi_{\max}|_{Re=1500}=0.116860$. For Erturk et al. [24]: $|\psi_{\max}|_{Re=1000}=0.117328$, $|\psi_{\max}|_{Re=1500}=0.116582$.

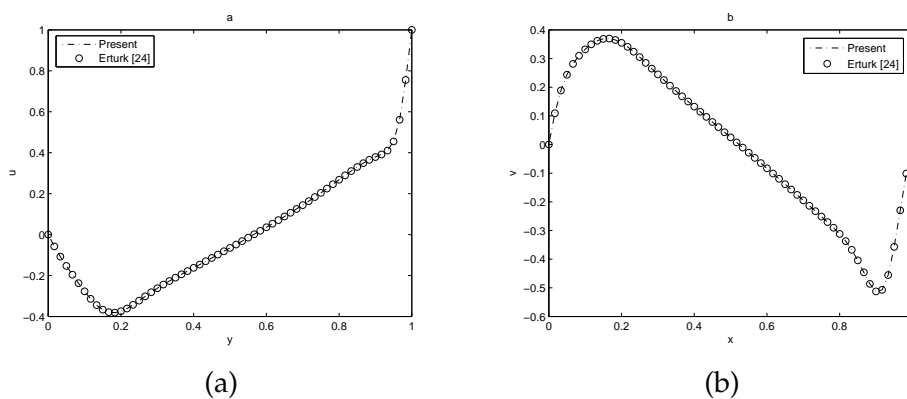


Figure 3: Comparison of the present velocity profiles in the absence of nanoparticles and internal heat generation with Erturk et al. [24] for $Re=1000$.

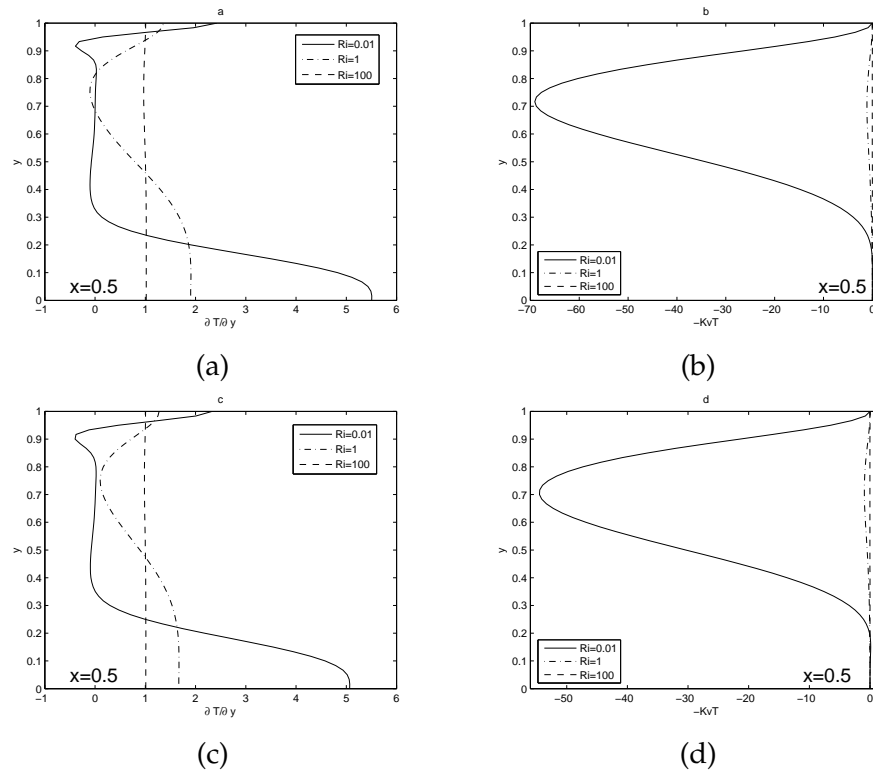


Figure 4: Vertical distributions of conduction ($\partial T / \partial y$) and convection ($-KvT$) along the mid-plane of the cavity for cases I with $\theta=0\%$ (a) and (b), $\theta=10\%$ (c) and (d).

To understand the heat transport processes associated with the upward and downward temperature gradients, the heat transfer rate along the vertical mid-plane is calculated through Eq. (7.1)

$$\frac{\partial T}{\partial y} - KvT. \tag{7.1}$$

The first and second terms of Eq. (7.1) denote the contributions due to conductive mode and convective mode, respectively [17]. Comparisons of the relative magnitude of each contribution along the mid-plane of the cavity for the stable and unstable temperature gradients are shown in Fig. 4. It can be seen that for the upward temperature gradient, the heat transfer is mainly through conduction, i.e., $\partial T / \partial y \approx 1$ and $-KvT \approx 0$ over nearly the entire region of the cavity when $Ri=100$. As Ri is decreased to 1.0, the conduction and convection almost have the same effect to the heat transfer, i.e., $\partial T / \partial y \approx -KvT$. When Ri is further decreased to 0.01, the conductive heat transport is significant in the regions and confined to a narrow region near the top ($0.9 \leq y \leq 1$) and bottom ($0 \leq y \leq 0.3$) walls and the substantial contribution of convective heat transport is observed in the interior region of the cavity, especially in the region ($0.6 \leq y \leq 0.8$). Similarly, to understand the heat

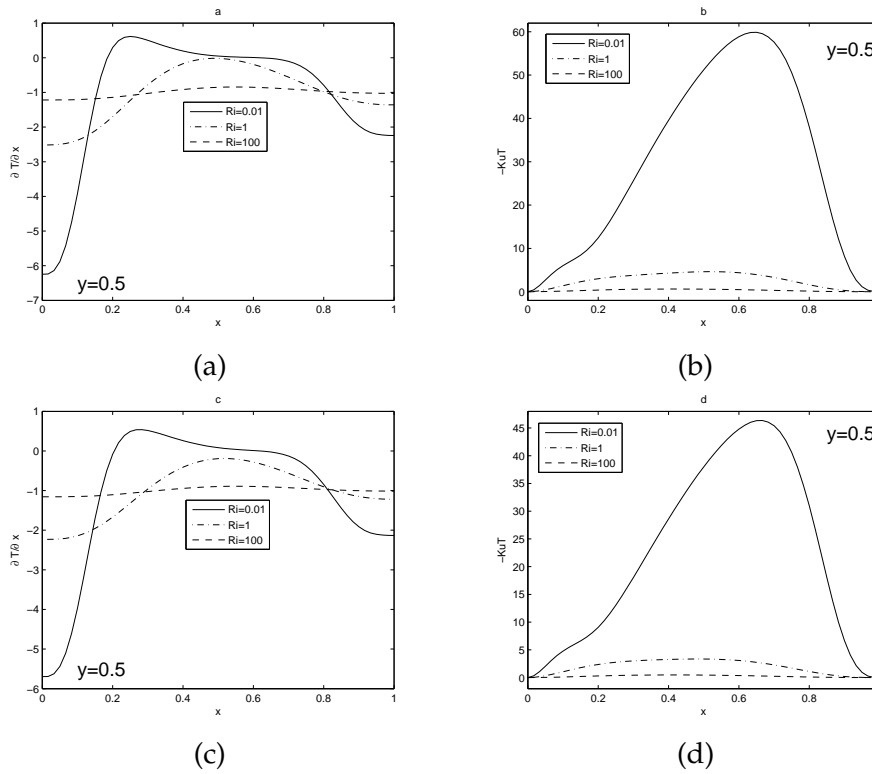


Figure 5: Horizontal distributions of conduction ($\partial T/\partial x$) and convection ($-KuT$) along the mid-plane of the cavity for cases II with $\theta=0\%$ (a) and (b), $\theta=10\%$ (c) and (d).

transport processes associated with the leftward and rightward temperature gradients, the heat transfer rate along the horizontal mid-plane is calculated through Eq. (7.2)

$$\frac{\partial T}{\partial x} - KuT. \tag{7.2}$$

Comparisons of the relative magnitude of each contribution along the mid-height of the cavity for the assisting and opposing-buoyancy cases are shown in Fig. 5. It can be seen that for the assisting buoyancy flow with $Ri = 100$, the contribution of the conductive mode is fixed ($\partial T/\partial x \rightarrow -1.2$) in the cavity, while the contribution of convective mode is relatively negligible ($-KuT \approx 0$). When the effect of shear force is increased ($Ri = 1$), the magnitude of conduction heat transfer equals nearly that of convection heat transfer in the interior region of the cavity. When $Ri = 0.01$, the conduction near the hot wall and the convection near the cold wall as well as in the interior region of the cavity increase remarkably. This fact suggests that for the strongly assisting buoyancy flow, the heat transport from the hot wall to the cold wall is through conduction near the hot wall convection in the bulk region, and a combination of conduction and convection near the cold wall.

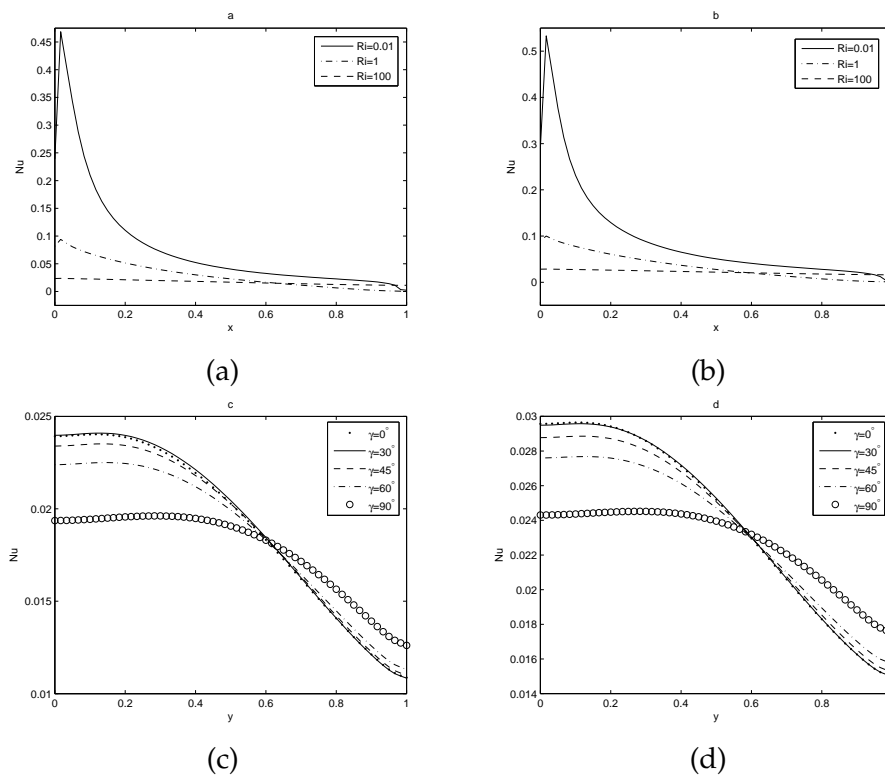


Figure 6: Local Nusselt numbers for different Richardson numbers (Ri) at top sidewall (a) and (b) for case I and different inclination angle (γ) at left sidewall (c) and (d) for case II with $\theta = 0\%$ (a) and (c) and $\theta = 10\%$ (b) and (d).

Fig. 6 illustrates the variations of the local Nusselt numbers Nu along the top sidewall at various Richardson numbers Ri for case I and the left sidewall at different inclination angle γ for case II. This indicates that the local heat transfer is directly affected by the temperature distribution on the surface. In other words, larger heat transfer occurs when the temperature is higher. When the natural convection dominates ($Ri = 100$), the local Nusselt numbers along the top sidewall gets no remarkable change on both sidewalls even if the nanoparticle volume fraction is increased. But, the local Nusselt numbers along the top sidewall increases much more rapidly for the forced convection dominated case ($Ri = 0.01$). This can be verified in Fig. 6(a) and (b). Fig. 6(c) and (d) illustrates the variations of the local Nusselt numbers along the left sidewall at various inclination angles γ . It is clearly observed from these figures that the local Nusselt number Nu decreases as γ increases on the lower half ($0 \leq y \leq 0.6$) while increases as γ decreases on the upper half ($0.6 \leq y \leq 1$). Moreover, increasing the volume fraction of nanoparticles also produce a significant enhancement of the local Nusselt number.

Figs. 7-9 present typical x -component of velocity u , y -component of velocity v and temperature T at the horizontal mid-plane of the cavity for various values of cavity in-

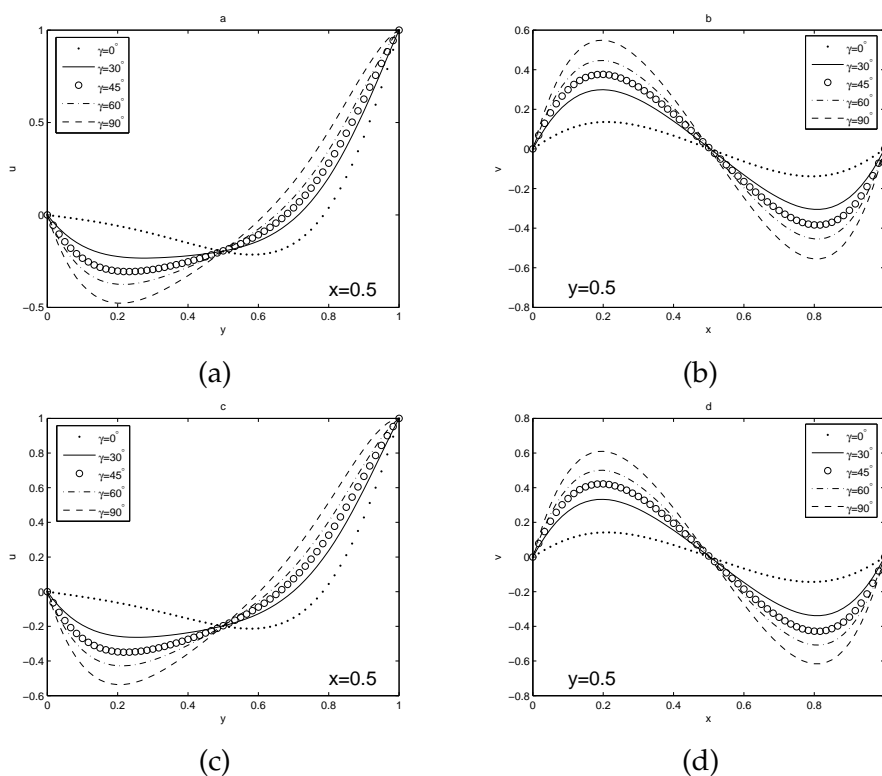


Figure 7: Typical profiles of x -component of velocity u (a) and (c) and y -component of velocity v (b) and (d) for various inclination angles γ and $Ri=100$, $\theta=0\%$ (a) and (b) and $\theta=10\%$ (c) and (d).

clination angles γ and different nanoparticle volume fractions θ . It is observed that the x -component of velocity u decreases in the bottom part of the cavity while it increases in the upper part of the cavity as the inclination angle increases in Figs. 6(a) and (c). On the other hand, the y -component of velocity v behaves exactly the opposite than the u velocity but the net velocity in the cavity decreases as γ increases in Fig. 7(b) and (d). Also, it is clear from Fig. 8 that the net velocity also decreases at the percent volume fraction of particles increases. In Fig. 9, the temperature profiles show that for case I, the temperature in the bottom part of the cavity decreases while it increases slightly in the region close to the moving wall as the nanoparticle volume fraction θ increases. The same behavior is predicted for case II. Also, the presence of the nanoparticles is predicted to increase the temperature in the bottom part of the cavity (for case I, $0 \leq x \leq 0.4$; for case II, $0 \leq y \leq 0.6$).

Figs. 10-12 show typical contour maps for the streamlines and isotherms obtained numerically for three values of the Richardson number Ri ($Ri=0.01, 1, 10$) at 0% (—) and 10% (⋯) particle volume fraction and three inclination angles ($\gamma=0^\circ, 45^\circ, 90^\circ$), respectively. As is clear from the definition of Ri , the value of the Richardson number provides a measure of the importance of buoyancy-driven natural convection relative to the lid-driven forced convection [5]. For the forced convection-dominated case ($Ri=0.01$), Figs. 10(a)

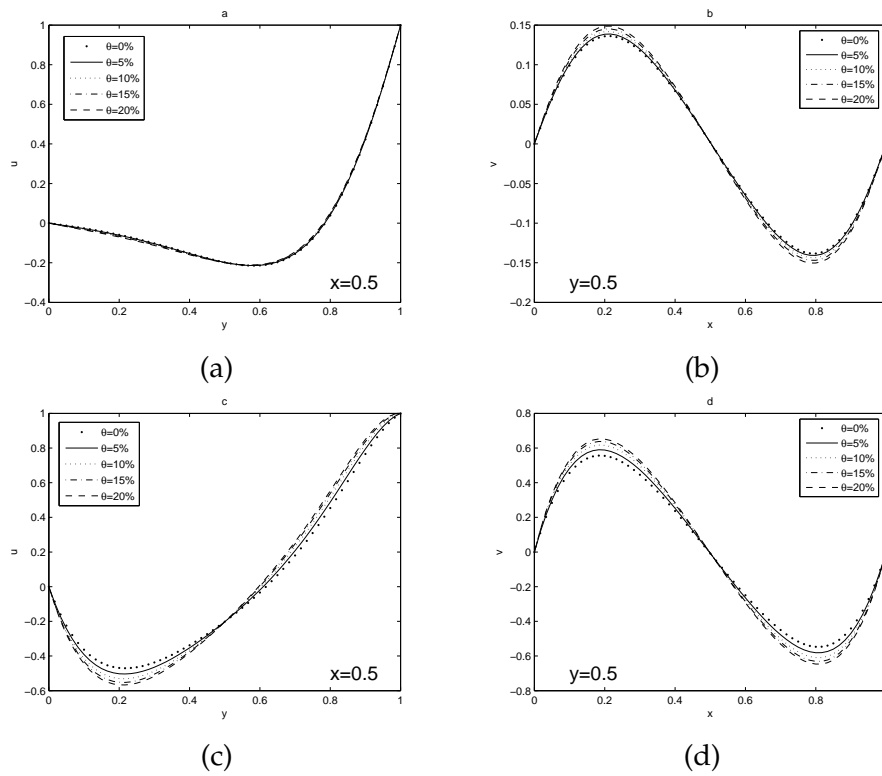


Figure 8: Typical profiles of x -component of velocity u (a) and (c) and y -component of velocity v (b) and (d) for different nanoparticle volume fractions θ and $Ri=100$, $\gamma=0^\circ$ for case I (a) and (b) and case II (c) and (d).

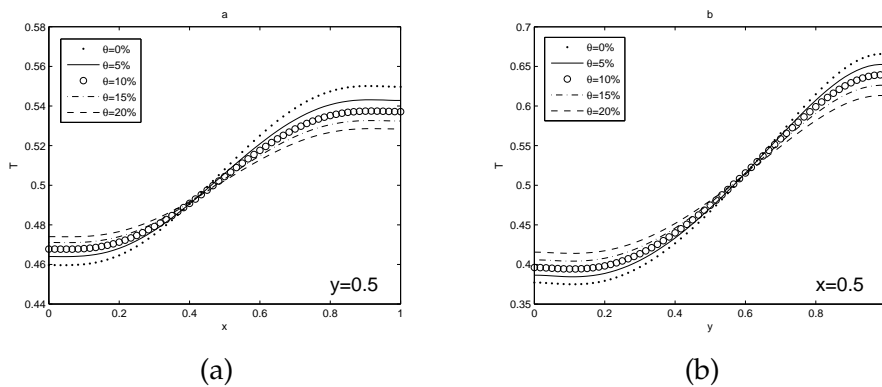


Figure 9: Typical profiles of temperature T for different nanoparticle volume fractions θ and $Ri=100$, $\gamma=0^\circ$ for case I (a) and case II (b).

and (b), Figs. 11(a) and (b) and Figs. 12(a) and (b) indicate that the buoyancy effect is overwhelmed by the mechanical effect of the sliding lid and the flow features are similar to those of a viscous flow of a non-stratified fluid in a lid-driven cavity. The streamlines

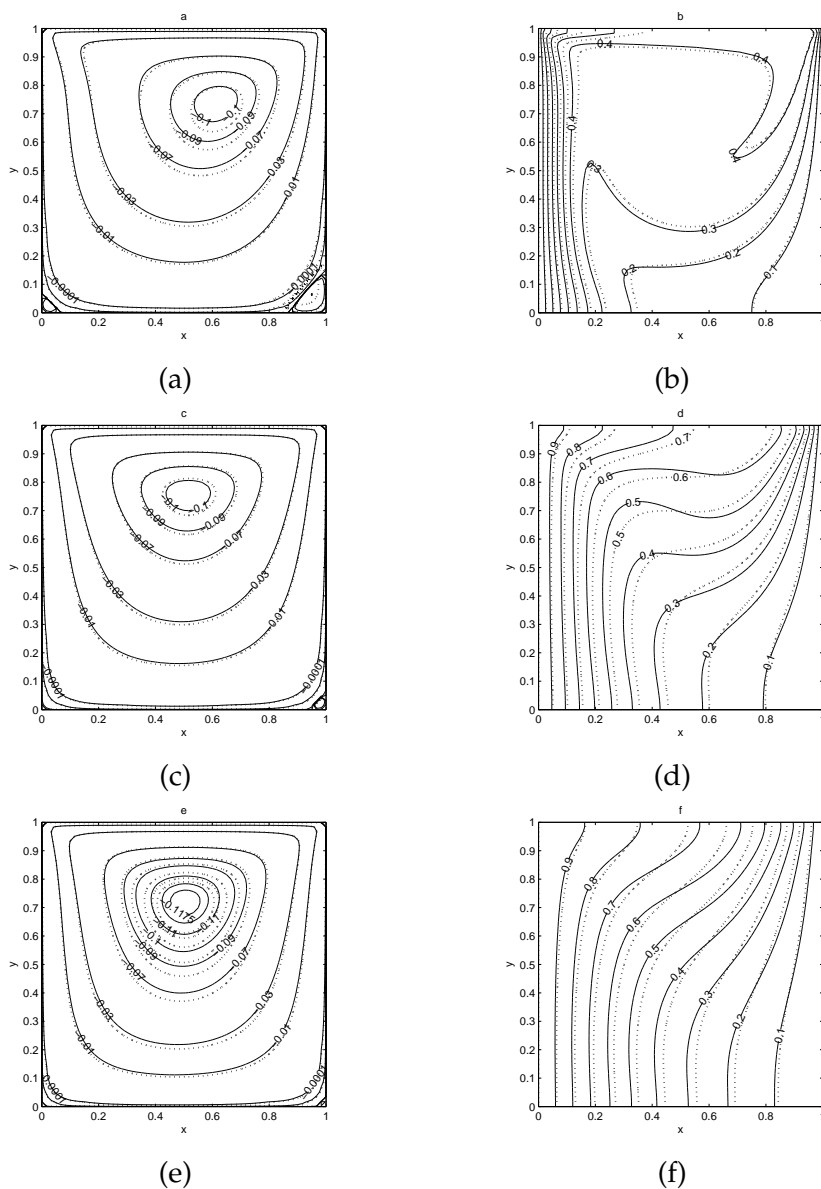


Figure 10: Streamline and isotherm contours for various Ri values (a) and (b) $Ri=0.01$ (c) and (d) $Ri=1$ (e) and (f) $Ri=100$ at $\gamma=0^\circ$, $\theta=0\%$ (—) and $\theta=10\%$ (···) for nanofluid: $|\psi_{\max}|_{Ri=0.01}=0.105179$, $|\psi_{\max}|_{Ri=1}=0.104403$, $|\psi_{\max}|_{Ri=10}=0.124530$.

behavior in a 2D lid-driven cavity is characterized by a primary recirculating cell occupying most of the cavity generated by the lid and two secondary eddies near the bottom wall corners with the one near the right bottom corner is bigger and stronger than the one in the left bottom corner of the cavity. The isotherms are clustered heavily near the

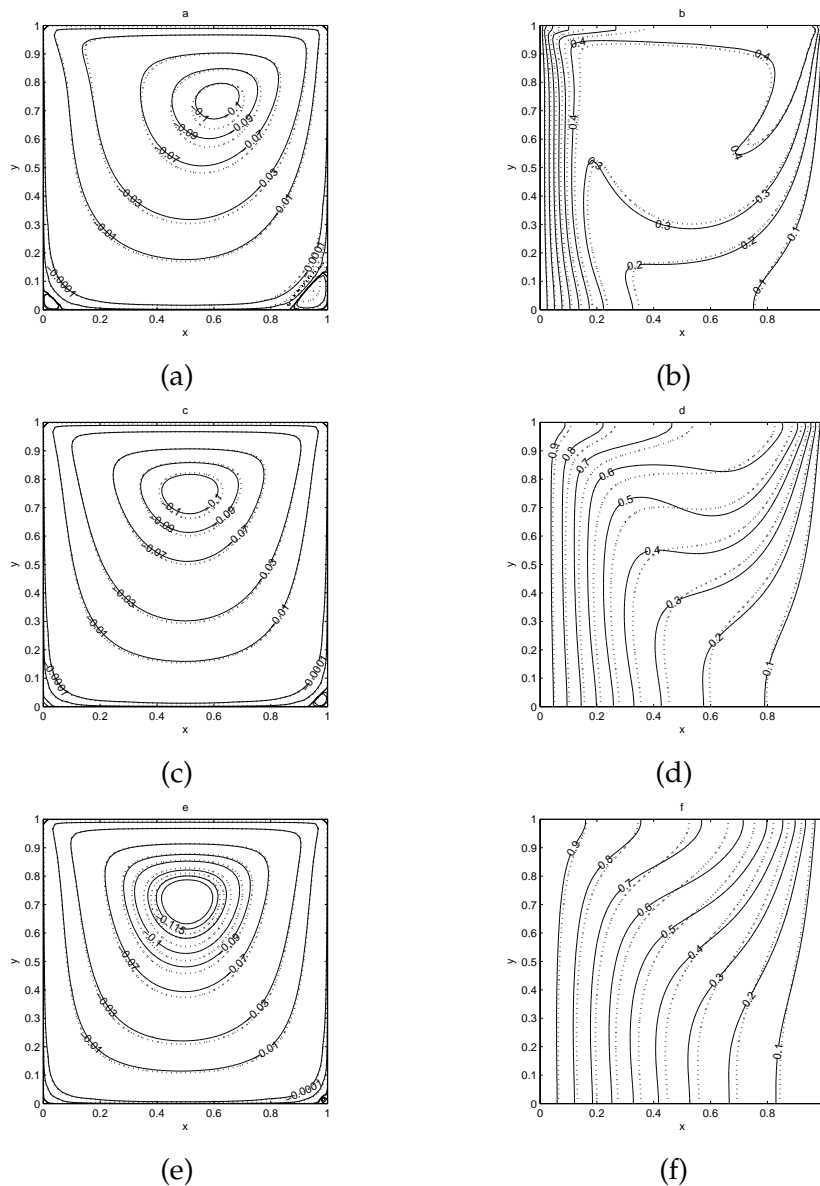


Figure 11: Streamline and isotherm contours for various Ri values (a) and (b) $Ri=0.01$ (c) and (d) $Ri=1$ (e) and (f) $Ri=10$ at $\gamma=45^\circ$, $\theta=0\%$ (—) and $\theta=10\%$ (---) for nanofluid: $|\psi_{\max}|_{Ri=0.01}=0.105261$, $|\psi_{\max}|_{Ri=1}=0.106598$, $|\psi_{\max}|_{Ri=10}=0.126930$.

left surface of the cavity which indicates steep temperature gradients in the horizontal direction in this region. In the remaining area of the cavity, the temperature gradients are weak and this implies that the temperature differences are very small in the interior region of the cavity due to the vigorous effects of the mechanically-driven circulations. As

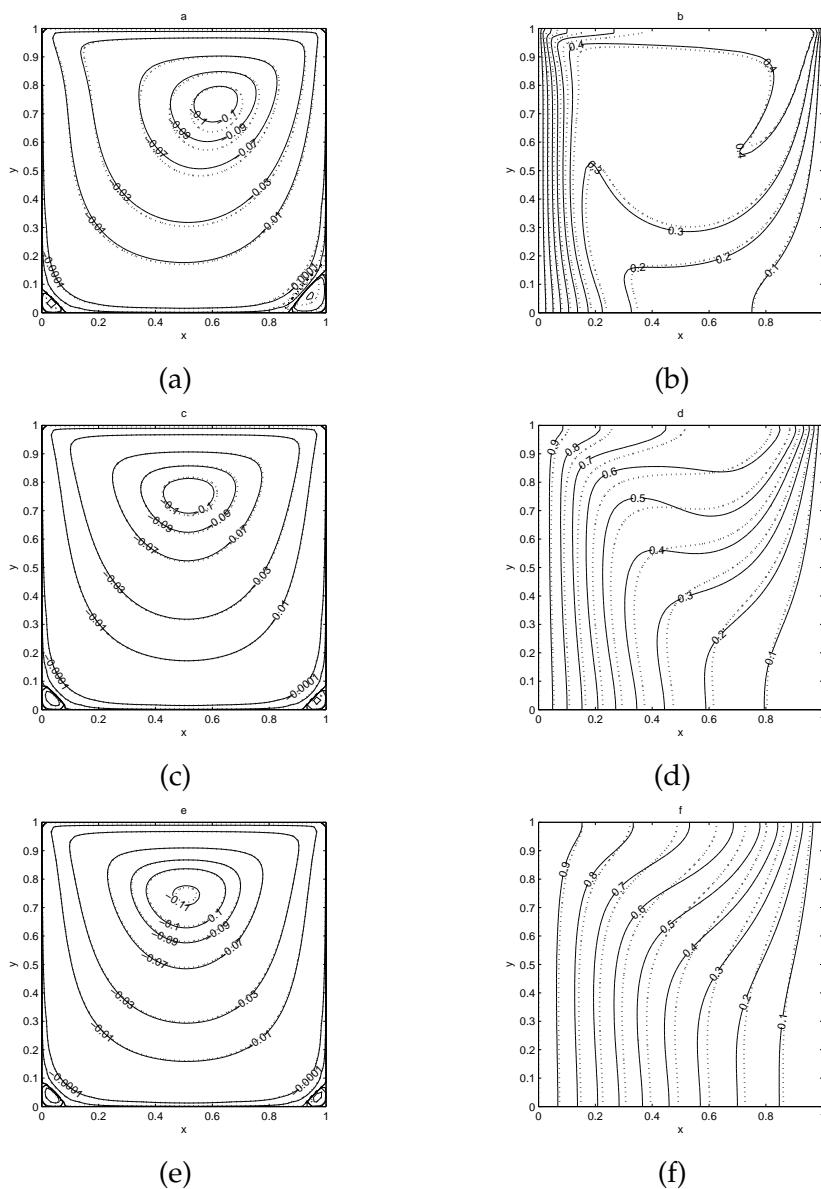


Figure 12: Streamline and isotherm contours for various Ri values (a) and (b) $Ri=0.01$ (c) and (d) $Ri=1$ (e) and (f) $Ri=10$ at $\gamma=90^\circ$, $\theta=0\%$ (—) and $\theta=10\%$ (⋯) for nanofluid: $|\psi_{\max}|_{Ri=0.01}=0.105254$, $|\psi_{\max}|_{Ri=1}=0.104833$, $|\psi_{\max}|_{Ri=10}=0.110739$.

the cavity is inclined ($\gamma=45^\circ$), the flow in the cavity slows down and the secondary eddies in the bottom corners becomes inhibited and of smaller size and the isotherms show no significant changes. For the mixed convection dominated case ($Ri=1$), Figs. 10(c) and (d), 11(c) and (d) and 12(c) and (d) indicate that the buoyancy effect is of relatively

comparable magnitude of the shear effect due to the sliding lid. The flow streamlines still show the formation of a primary recirculating cell of the size of the cavity generated by the lid and two smaller secondary eddies near the bottom corners. The core of the primary cell moves towards the top moving wall. The isotherms spread leftward indicating moderate temperature gradients in the horizontal direction. Increasing the cavity inclination angle γ , causes the primary cell to rotate at a slower rate while the two secondary eddies disappear. The isotherm contours look similar to the case of non-inclined cavity ($\gamma = 0^\circ$), but with increased temperature gradients at the left wall. For the natural convection dominated case ($Ri = 10$), the buoyancy effect is dominant and the streamlines are almost stagnant in the bulk of the cavity interior except at portions close to the sliding top wall. The isotherms spread further leftward showing less distortion than the isotherms corresponding to $Ri = 1$. Similar to the case of $Ri = 1$, inclining the cavity results in flow retardation and increased temperature gradients along the left wall of the cavity. This is clear from Figs. 10(e) and (f), 11(e) and (f) and 12(e) and (f). As for the effect of the nanoparticle volume fraction θ , one can see that an increase in solid volume fraction ($\theta = 10\%$) generates a decrease in the values of ψ_{\max} . The fluid, therefore, moves slower in the cavity in the presence of nanoparticles. As far as the temperature distribution is concerned, clear differences are observed in the isotherm contour plots compared to the case $\theta = 0\%$ (pure water). These differences are accentuated as the solid volume fraction increases and indicate that the presence of nanoparticles have significant effect on the heat transfer rate through the cavity.

8 Conclusions

We employ an algorithm that is uniformly fourth-order accurate and compact in the discretization of the governing equations, treatment of the boundary conditions and source term resolution for solving the 2D incompressible steady laminar mixed convective flow and heat transfer of a nanofluid made up of water and Al_2O_3 in a lid-driven inclined square enclosure. The no-heat-flux boundary condition at the adiabatic walls has been imposed through a special strategy taking care to maintain compactness at higher accuracy. This technique has the potential of being extended to other similar physical situations. The work also achieves HOC resolution of the source term and its easy assimilation into the solution procedure. Use of pseudo-time algorithms to solve the HOC finite difference schemes makes the solution procedure robust. The method is validated by direct comparisons with previously published work on special cases of the problem and the results are found to be in good agreement. Graphical results for various parametric conditions were presented and discussed. It was found that the heat transfer mechanisms and the flow characteristics inside the cavity are strongly dependent on the Richardson number. Also, it was predicted that significant heat transfer enhancement could be obtained due to the presence of nanoparticles and that this was accentuated by inclination of the enclosure at moderate and large Richardson numbers.

Acknowledgments

This work is supported by the National Natural Science Foundation of China (No. 10971159).

References

- [1] S. U. S. CHOI, *Enhancing thermal conductivity of fluids with nanoparticle*, ASME FED, 231 (1995), pp. 99–105.
- [2] J. A. EASTMAN, S. U. S. CHOI, S. LI, W. YU AND L. J. THOMPSON, *Anomalously increased effective thermal conductivities of ethylene glycol-based nanofluids containing copper nanoparticles*, Appl. Phys. Lett., 78 (2001), pp. 718–720.
- [3] H. XIE, J. WANG, T. G. XIE, Y. LIU AND F. AI, *Thermal conductivity enhancement of suspensions containing nanosized alumina particles*, J. Appl. Phys., 91 (2002), pp. 4568–4572.
- [4] C. J. HO, M. W. CHEN AND Z. W. L, *Numerical simulation of natural convection of nanofluid in a square enclosure: effects due to uncertainties of viscosity and thermal conductivity*, Int. J. Heat Mass Trans., 51 (2008), pp. 4506–4516.
- [5] E. ABU-NADAA AND A. J. CHAMKHA, *Mixed convection flow in a lid-driven inclined square enclosure filled with a nanofluid*, Euro. J. Mech., 29 (2010), pp. 472–482.
- [6] S. KUMAR, S. K. PRASAD AND J. BANERJEE, *Analysis of flow and thermal field in nanofluid using a single phase thermal dispersion model*, Appl. Math. Model., 34 (2010), pp. 573–592.
- [7] S. K. DAS, S. U. S. CHOI AND H. E. PATEL, *Heat transfer in nanofluids: a review*, Heat Trans. Eng., 37 (2006), pp. 3–19.
- [8] X. Q. WANG AND A. S. MUJUMDAR, *Heat transfer characteristics of nanofluids: a review*, Int. J. Thermal Sci., 46 (2007), pp. 1–19.
- [9] K. KHANAFER, K. VAFAI AND M. LIGHTSTONE, *Buoyancy driven heat transfer enhancement in a two-dimensional enclosure utilizing nanofluids*, Int. J. Heat Mass Trans., 46 (2003), pp. 3639–3653.
- [10] R. Y. JO AND S. C. TZENG, *Numerical research of nature convective heat transfer enhancement filled with nanofluids in rectangular enclosures*, Int. Commun. Heat Mass Trans., 33 (2006), pp. 727–736.
- [11] J. IMBERGER AND P. F. HAMBLINA, *Dynamics of lakes, reservoirs and cooling ponds*, Rev. Fluid Mech., 14 (1982), pp. 153–187.
- [12] F. J. K. IDERIAH, *Prediction of turbulent cavity flow driven by buoyancy and shear*, J. Mech. Eng Sci., 22 (1980), pp. 287–295.
- [13] K. TORRANCE, R. DAVIS, K. ELIKE, P. GILL, D. GUTMAN, A. HSUI, S. LYONS AND H. ZIEN, *Cavity flows driven by buoyancy and shear*, J. Fluid Mech., 51 (1972), pp. 221–231.
- [14] R. IWATSU, J. M. HYUN AND K. KUWAHARA, *Mixed convection in a driven cavity with a stable vertical temperature gradient*, Int. J. Heat Mass Trans., 36 (1993), pp. 1601–1608.
- [15] R. K. TIWARI AND M. K. DAS, *Heat transfer augmentation in a two-sided lid-driven differentially heated square cavity utilizing nanofluids*, Int. J. Heat Mass Trans., 50 (2007), pp. 2002–2018.
- [16] M. MUTHAMILSELVAN, P. KANDASWAMY AND J. LEE, *Heat transfer enhancement of copper-water nanofluids in a lid-driven enclosure*, Commun. Nonlinear Sci. Numer. Simul., 15 (2009), pp. 1501–1510.
- [17] T. S. CHENG AND W. H. LIU, *Effect of temperature gradient orientation on the characteristics of mixed convection flow in a lid-driven square cavity*, Comput. Fluids, 39 (2010), pp. 965–978.

- [18] R. IWATSU, J. M. HYUN AND K. KUWAHARA, *Mixed convection in a driven cavity with a stable vertical temperature gradient*, Int. J. Therm. Sci., 36 (1993), pp. 1601–1608.
- [19] E. ABU-NADA, *Effects of variable viscosity and thermal conductivity of Al_2O_3 -water nanofluid on heat transfer enhancement in natural convection*, Int. J. Heat Fluid Flow, 30 (2009), pp. 679–690.
- [20] W. F. SPÖTZ AND G. F. CAREY, Texas Institute of Computational and Applied Mechanics Technical Report No. 94-03, 1994 (unpublished).
- [21] J. C. KALITA, D. C. DALAL AND A. K. DASS, *Fully compact higher-order computation of steady-state natural convection in a square cavity*, DOI: 10.1103/PhysRevE.64.066703.
- [22] J. C. KALITA, D. C. DALAL AND A. K. DASS, *A class of higher order compact schemes for the unsteady two-dimensional convection-diffusion equation with variable convection coefficients*, Int. J. Numer. Methods Fluids, 38 (2002), pp. 1111–1131.
- [23] S. C. R. DENNIS AND J. D. HUDSON, *Compact h^4 finite-difference approximations to operators of Navier-Stokes type*, J. Comput. Phys., 85 (1989), pp. 390–416.
- [24] E. ERTURK AND C. GÖKCÖL, *Fourth order compact formulation of Navier-Stokes equations and driven cavity flow at high Reynolds numbers*, Int. J. Numer. Methods Fluids, 50 (2006), pp. 421–436.
- [25] G. DE VAHL DAVIS AND I. P. JONES, *Natural convection in a square cavity: a comparison exercise*, Int. J. Numer. Methods Fluids, 3 (1983), pp. 227–248.
- [26] M. HORTMANN AND M. PERIIC, *Finite volume multigrid prediction of laminar natural convection: benchmark solutions*, Int. J. Numer. Methods Fluids, 11 (1990), pp. 189–207.
- [27] Z. F. TIAN AND Y. B. GE, *A fourth-order compact finite difference scheme for the steady streamfunction-vorticity formulation of the Navier-Stokes/ Boussinesq equations*, Int. J. Numer. Methods Fluids, 41 (2003), pp. 495–518.
- [28] E. ERTURK, T. C. CORKE AND C. GÖKCÖL, *Numerical solutions of 2-D steady incompressible driven cavity flow at high Reynolds numbers*, Int. J. Numer. Methods Fluids, 48 (2005), pp. 747–774.
- [29] T. V. S. SEKHAR, B. H. S. RAJU AND Y. V. S. S. SANYASIRAJU, *Higher-order compact scheme for the incompressible Navier-Stokes equations in spherical geometry*, Commun. Comput. Phys., 11 (2012), pp. 99–113.
- [30] L. CHEN, J. SHEN AND C. XU, *Spectral direction splitting schemes for the incompressible Navier-Stokes equations*, East Asian J. Appl. Math., 1 (2011), pp. 215–234.
- [31] C. CHEN, M. REN, A. SRINIVANSAN AND Q. WANG, *3-D numerical simulations of biofilm flows*, East Asian J. Appl. Math., 1 (2011), pp. 197–214.
- [32] D. W. PEACEMAN AND H. H. RACHFORD, *The numerical solution of parabolic and elliptic differential equations*, J. Soc. Ind. Appl. Math., 3 (1995), pp. 28–41.
- [33] R. S. HIRSH, *Higher order accurate difference solutions of fluid mechanics problems by a compact differencing technique*, J. Comput. Phys., 19 (1975), pp. 90–109.
- [34] P. N. SHANKAR AND M. D. DESHPANDE, *Fluid mechanics in the driven cavity*, Annu. Rev. Fluid Mech., 32 (2000), pp. 93–136.
- [35] U. GHIA, K. N. GHIA AND C. T. SHIN, *High-resolutions for incompressible Navier-Stokes equation and a multigrid method*, J. Comput. Phys., 48 (1982), pp. 387–411.
- [36] J. ZHANG, *Numerical simulation of 2D square driven cavity using fourth-order compact finite difference schemes*, Comput. Math. Appl., 45 (2003), pp. 43–52.
- [37] O. BOTELLA AND R. PEYRET, *Benchmark spectral results on the lid-driven cavity flow*, Comput. Fluids, 27 (1998), pp. 421–433.
- [38] C. H. BRUNEAU AND M. SAAD, *The 2D lid-driven cavity problem revisited*, Comput. Fluids, 35 (2005), pp. 326–348.